PHYSICAL REVIEW B **111**, 184426 (2025)

Growth-induced magnetic anisotropy in Co/C_{60} bilayers: Insights from a two-grain Stoner-Wohlfarth model

Sonia Kaushik,[1,*,†] Rakhul Raj,[1,*] Pooja Gupta,[2,3] Andrei Chumakov,[4] Matthias Schwartzkopf,[4]
V. Raghavendra Reddy,[1] and Dileep Kumar[1,‡]
[1] *UGC-DAE Consortium for Scientific Research, Khandwa Road, Indore-452001, India*
[2] *Synchrotron Utilization Division, RRCAT, Indore-452013, India*
[3] *Homi Bhabha National Institute, Training School Complex, Anushakti Nagar, Mumbai 400094, India*
[4] *Deutsches Elektronen-Synchrotron, DESY, Notkestraße 85, 22607 Hamburg, Germany*

(Received 17 October 2024; revised 2 February 2025; accepted 6 May 2025; published 20 May 2025)

Organic spintronics has gained significant interest within the scientific community due to its potential applications in spin-valve devices. However, the realization of an efficient room-temperature organic spin-valve device remains elusive, primarily due to the complex spin transport at metal-organic interfaces. Hence, the study of these metal-organic bilayer interfaces is essential for the conception of such devices. This study investigates the Co-C_{60} interface and its impact on the magnetic properties of the Co layer. We examine the structural and magnetic properties of ultrathin cobalt (Co) films deposited on a fullerene (C_{60}) layer to understand the origin of magnetic anisotropy in metal-organic bilayer structures. The penetration of ferromagnetic Co atoms into the C_{60} film is confirmed through x-ray reflectivity and secondary-ion-mass spectroscopy. Additionally, grazing incidence small-angle x-ray scattering and atomic force microscopy provide ample insights into the morphological properties of the Co/C_{60} bilayers. Grazing incidence x-ray diffraction and grazing incidence wide-angle x-ray scattering confirm the texturing of Co in the bilayer at higher cobalt thicknesses. Angular-dependent magneto-optic Kerr effect hysteresis measurements, with varying Co layer thicknesses, reveal information about growth-induced uniaxial magnetic anisotropy. Unlike inorganic silicon substrates, where Co texturing and magnetic anisotropy are absent, magnetic anisotropy in Co films begins to develop at a thickness of 25 Å on the C_{60} layer and increases with further cobalt deposition. This texturing induces a dispersion in magnetic anisotropy, leading to an anomalous increase in coercivity and remanence along the hard axis. The anomalous behavior in coercivity and remanence variation along the nominal hard axis is explained by the two-grain Stoner-Wohlfarth model and is further corroborated by the nonuniform spatial distribution of magnetic domains observed through Kerr microscopy. Our simulations show that these magnetic anomalies arise due to the formation of local energy minima in the energy landscape near the nominal hard axis.

DOI: 10.1103/PhysRevB.111.184426

I. INTRODUCTION

The study of ferromagnetic-organic material (FM-OM) thin-film nanostructures has gained considerable attention due to their unique physical phenomena and potential applications in organic spintronic devices [1,2]. Based on organic semiconductors (OSC), these structures offer advantages such as low spin-orbit coupling, reduced hyperfine interactions, and long spin lifetime. Additionally, OSC-based devices are cost effective and mechanically flexible, making them promising candidates for future organic spintronics applications [2,3]. The various FM layers (such as FeCoB [4], Fe [5–9], Co [10,11], and FeNi [12]) have been combined with organic material layers (C_{60}, Alq_3, rubrene, and pentacene) over the past decade to achieve controlled magnetoresistance and giant spin polarization [10,13–15]. Among these combinations, C_{60}-based FM-OM thin-film structures are particularly significant due to the potential for significant room-temperature magnetoresistance [16,17]. Considerable progress has been made in understanding spin injection, manipulation, and detection in FM-OM thin-film structures but a comprehensive experimental understanding is still lacking. One of the primary reasons for this might be the mechanical softness of OSC that leads to the FM metal atom penetration, potential chemical reactions, and complex magnetism at the interfaces. Various studies have been performed in the literature involving the impact of these interfaces on the magnetic properties of the FM electrodes such as magnetization, magnetic anisotropy, magnetic dead layer, and coercivity [6,18–21].

Magnetic anisotropy is one of the important properties of FM-OSC based structures; it plays a vital role in controlling the performance and operation of these organic spin valves and determines the magnetic functionality of the devices [22,23]. In the case of epitaxial magnetic thin films, uniaxial magnetic anisotropy (UMA) is often realized when deposited on various single-crystal substrates such as Ag (001), Cu (100), MgO (100), and $SrTiO_3$ (001) [24–26]. However,

---

[*] These authors contributed equally to this work.
[†] Contact author: soniakaushik1996@gmail.com
[‡] Contact author: dkumar@csr.res.in

spin-orbit coupling originated through ordered crystallographic structure is responsible for the preferred magnetization direction with respect to the crystal structure giving rise to intrinsic magnetocrystalline anisotropy. Unlike inorganic layered structures, where the epitaxy is due to the lattice-matched substrates underneath, the growth of metallic thin films on organic material is either amorphous or polycrystalline in nature due to lattice mismatching and diffusion at the interfaces. Hence, unlike the impact of adsorbed organic layer on the magnetic anisotropy of bottom FM electrodes, the origin and interfacial effect in UMA of top FM would be quite different. Thus, the goal of the current study is to establish correlations between these magnetic properties and the evolving structure and morphology during FM film growth on an organic layer.

Moreover, polycrystalline and amorphous films do not exhibit long-range structural order [27]. Therefore, the origin of the UMA in polycrystalline Co films on inorganic silicon substrates is the stress associated during film growth [28,29]. Contrary to this, the origin of UMA in organic material-based bilayer structures is related to the morphology and surface roughness. Bergenti *et al.* grew Co thin films by rf sputtering on Tris(8-hydroxyquinoline) aluminium (Alq_3) layers and suggested the cause of UMA in Co film is attributed to the morphology of the Alq_3 layer underneath [30]. Studies have been conducted in the literature where the role of the magnetic anisotropy has been investigated in the performance of the organic spin-valve devices [31]. Despite the vast importance of magnetic anisotropy in the performance of spin valve, very little work has been reported in understanding the magnetic anisotropy and magnetization reversal mechanism of the top FM films deposited on the organic layers.

The present work provides a deep insight into the origin of unconventional uniaxial magnetic anisotropy in Co/C_{60} bilayers. In contrast to previous studies lacking thickness dependence, current research examines a series of bilayers in ultrathin-film regime of Co layer, ensuring consistent morphology within the bilayers due to identical preparation conditions. The morphological and structural investigations confirm the preferential orientation of the Co film along hexagonal-close-packed (hcp) (002) in the film plane. Further, the magnetic investigations deduce the dispersion in the magnetic anisotropy axis. The unusual behavior in the magnetic anisotropy and magnetization reversal mechanism observed via Kerr microscopy is explained utilizing the two-grain Stoner-Wohlfarth model. With the help of simulations, we elucidate that the observed magnetic anomalies near the hard axis are caused by the formation of local minima in the energy contour plots. The unconventional behavior in the magnetic properties of Co film is mainly attributed to the Co-C_{60} interface.

II. EXPERIMENT

A set of four Co/C_{60} bilayers and corresponding reference samples (Co on bare silicon substrate) were prepared by depositing Co films of nominal thicknesses 10, 25, 40, and 180 Å. These samples will be denoted as S1, S2, S3, and S4 and the corresponding reference samples as $S1_{ref}$, $S2_{ref}$, $S3_{ref}$, and $S4_{ref}$, respectively, in the paper. The thin capping layer of aluminum (Al) having a thickness of 20 Å was deposited to prevent the oxidation of Co film. Metallic films were prepared using high-power impulse magnetron sputtering under a base pressure of 1.33×10^{-7} mbar, whereas the C_{60} layer was deposited on a silicon substrate via sublimation of C_{60} powder supplied by Sigma-Aldrich (99.9% purity) at a rate of 0.2 Å/s using a homemade thermal evaporator under base pressure of 10^{-7} mbar. The thicknesses of the Co layers in the samples for this study were determined at different growth regimes based on our previous work, where *in situ* transport measurements were performed during the growth of the Co film to correlate the thickness with different Volmer-Weber growth regimes [11]. The structural parameters such as thickness, roughness, and density of the films were obtained using x-ray reflectivity (XRR) carried out using a Bruker D8 diffractometer using x-rays of 8.047-keV energy. Synchrotron-based x-ray diffraction (XRD) measurements were carried out at BL02 beamline (Indus 2, RRCAT, Indore) in out-of-plane (OP-XRD) and in-plane (IP-XRD) geometry at 15-keV energy. Depth-profiling measurements were carried out using secondary-ion-mass spectroscopy using O_2^+ ions to sputter out the film with energy (30 keV, current 30 nA) in the sample area of around 100 × 100 µm². For the topographical analysis and surface roughness measurement of the samples, atomic force microscopy (AFM) measurements in tapping mode were performed at room temperature using Bruker's Bioscope Resolve system. The silicon cantilever with nominal spring constant of 50 N/m and resonant frequency around 290 kHz was used for imaging. Scanning electron microscope (SEM) measurements were also performed in conventional geometry using Axia ChemiSEM by Thermofisher Scientific. To understand the morphological information of the surface and the buried layers, grazing incidence small-angle x-ray scattering (GISAXS) measurements were carried out simultaneously with grazing incidence wide-angle x-ray scattering (GIWAXS) at P03 beamline (synchrotron PETRA III, DESY, Hamburg, Germany), using photon energy of 12.11 keV with a beam size of 35 × 25 µm² (horizontal-to-vertical ratio). The sample-to-detector distance (SDD) was set to 214 mm, and the LAMBDA 9M pixel detector (X-Spectrum ©) with pixel size of 55 × 55 µm² was used for GIWAXS measurements, while PILATUS 2M pixel detector (Dectris AG) (172 × 172 µm²) was kept at the SDD of 4280 mm for GISAXS measurements. Magnetic hysteresis loops and the domain imaging of the samples were carried out using the Kerr microscopy-based magneto-optic Kerr effect (MOKE) measurements in longitudinal geometry. The loops were recorded by varying the in-plane azimuthal angle (ϕ) from 0° to 360° to investigate magnetic anisotropy in the samples.

III. RESULTS AND DISCUSSION

A. X-ray reflectivity

The growth of the C_{60} layer on silicon substrates was studied and the thickness, roughness, and density of the layer was determined using XRR measurements; the morphological characterizations were carried out using AFM and GISAXS measurements discussed in the Supplemental Material [32]. The polycrystalline behavior of the C_{60} film was confirmed by GIWAXS measurements [32]. Figures 1(a)–1(d) show

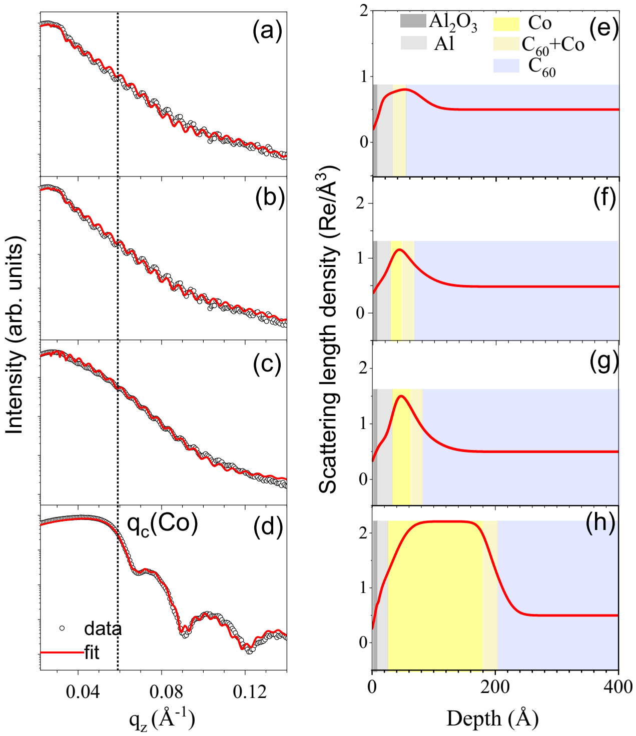

FIG. 1. (a)–(d) X-ray reflectivity pattern: circles represent the experimental data and solid line represents the fitted data; (e)–(h) scattering length density profile of the samples S1, S2, S3, and S4, respectively. Here, Co, C_{60}, Al, and Al_2O_3 are used to represent the cobalt, fullerene, aluminum, and aluminum oxide layer in the samples, respectively.

the XRR patterns of all samples (S1–S4), which are plotted against the scattering vector $q_z = 4\pi \sin\theta/\lambda$ on the x axis, where θ is the incident angle and λ is the wavelength of the x-ray. The periodic oscillations (Kiessig fringes) in all the XRR patterns are due to the thickness of the total structure [33]. In the case of the S4 sample, broad and short periodic oscillations in the XRR pattern correspond to the Co and total thickness (Al + Co + C_{60}), respectively. The difference between two periodic oscillations is inversely proportional to the thickness of the layer ($d = 2\pi/\Delta q$), where d is the film thickness. It is to be noted that the broad oscillations are not visible in the case of the ultrathin Co layers. The more damping in the oscillations at the lower thickness of Co (sample S1, S2, and S3) is attributed to the rough interface due to the deep penetration of Co metal atoms into the C_{60} layer [34].

All XRR patterns are fitted using GENX software based on Parratt formulism to extract the structural parameters of all the samples [35,36]. The obtained values of thickness and density (ρ) of the Co film are shown in Table I. Compared to the reference samples [32], the best fit to the XRR data is obtained by considering two different layers (Co_{top} and Co_{int}) of Co film with varying densities. Co_{int} layers have lower values of ρ in all samples due to Co diffusion in the C_{60} layer near the interface. In the case of S1, XRR was fitted by considering the whole Co layer as the Co_{int} layer having reduced density of 4.1 g/cm³. It is mainly due to the lower deposited thickness of Co film; complete Co film gets diffused inside the C_{60} layer. For samples S2–S4, on the top of Co_{int} layer having 20-Å thickness, another layer denoted as Co_{top} is formed whose thickness and density increases on increasing the deposition thickness of Co film. The density of Co_{top} in samples S2 and S3 is comparatively less than the Co bulk material ($Co_{bulk} \sim 8.9\,g/cm^3$), which indicates that the Co_{top} layer is not entirely continuous.

TABLE I. Thickness and density of Co film obtained from XRR fitting. Errors in layer thicknesses are ±5 Å.

	Co_{top}		Co_{int}	
Sample	d (Å)	ρ (g/cm³)	d (Å)	ρ (g/cm³)
S1			19	4.1
S2	18	5.2	20	4.1
S3	30	6.0	20	4.1
S4	153	8.9	20	6.2

On the other hand, the density of the Co_{top} layer for S4 is almost the same as the Co bulk material, confirming the formation of a continuous layer on the C_{60} film. One may note that if we consider the real scenario of the Co/C_{60} bilayers, instead of forming a separate intermixing layer, there is a gradient in the density of the Co film due to the penetration of the Co atoms inside the C_{60} layer. Since the Co deposition thickness is much higher in sample S4 as compared to samples S1–S3, higher density of the interfacial Co layer is obtained in sample S4. These results are in accordance with the earlier *in situ* work [11], where Co film grows on C_{60} via diffused small-sized isolated islands in the C_{60} matrix at the interface. These isolated islands grow larger to connect with other islands, which combine to form a continuous film at a higher thickness, around 75 Å. The XRR data fit reveals information regarding the diffusion of the Co clusters inside C_{60} at the interface, which is also confirmed by the elemental depth profiles observed in the secondary-ion-mass spectroscopy measurements [32].

B. Synchrotron-based grazing incidence small-angle x-ray scattering

The morphological and structural characterization of the samples are carried out using simultaneous GISAXS and GIWAXS measurements. The schematic of the experimental geometry used for simultaneous GISAXS and GIWAXS measurements at P03 beamline, PETRA III is shown in Fig. 2. Here, k_i and k_f denote the incident and reflected wave vectors, α_i is the incidence angle, and α_f and $2\theta_f$ are the exit angle and in-plane scattering angles, respectively. In two-dimensional GISAXS images, horizontal line cuts taken at the Yoneda peak region along the q_y direction provide information on the lateral structures of the material parallel to the film surface, while the off-specular vertical cut along q_z offers information on the structure perpendicular to the substrate [37].

Two-dimensional (2D) GISAXS images of the samples are shown in Figs. 3(a)–3(d), respectively. The resulting GISAXS patterns depend on the size, shape, and arrangement of the nanostructured layer. The position of the direct beam

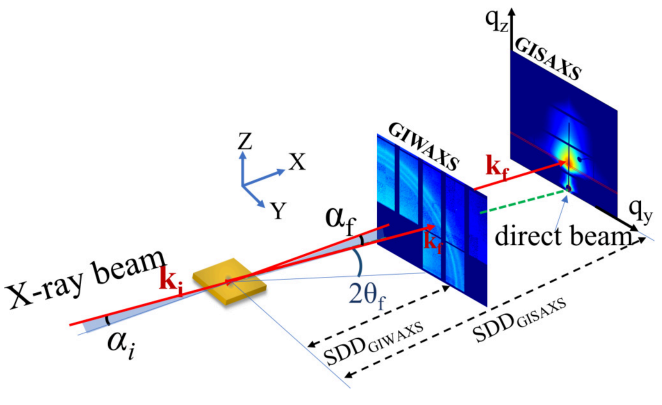

FIG. 2. Schematic of the geometry of the experiment for simultaneous GISAXS and GIWAXS measurements at P03 beamline, Petra III.

stop, specular beam stop, and intermodular gap are marked along with the position of the horizontal and vertical cuts in Fig. 3(a). The Yoneda peak position for Co and C_{60} is also marked in Fig. 3(c). The observed GISAXS pattern for sample S4 [shown in Fig. 3(d)] shows the regular intensity stripe features in the out-of-plane direction due to the parallel orientation of Co and C_{60} layers to the substrate.

The line profiles of $I(q_y)$ and $I(q_z)$ extracted for qualitative analysis of the GISAXS data using the DPDAK software [38] are shown in Figs. 3(e) and 3(f), respectively. The cuts along the q_y and q_z directions contain information about the sample's lateral and vertical structural parameters. In Fig. 3(e), the broad hump at $q_y = 0.00875\ \text{Å}^{-1}$, which is marked by dotted lines, does not shift significantly on depositing the Co film. Thus, this can explicitly correspond to the larger domains of C_{60} molecules with a lateral size $(2\pi/q_y)$ of around 718 Å, which becomes decorated by Co. Additionally, a small peak appears at larger q_y values for samples S1–S4 which shifts to lower q values as Co thickness increases. Due to the maxima in the interference function, this peak is related to the cluster correlation distances or average interparticle distances (D) between two neighboring clusters [39,40]. Further, the broadening in the peak indicates the distribution in the interparticle distances occurring due to the random arrangement of the Co clusters on the C_{60} layer. This peak appears at q_y value larger than 0.1 Å^{-1} for samples S1 and S2. This suggests that the average interparticle distance between the neighboring Co clusters is smaller than 63 Å. This can be understood as due to the high surface energy of Co: The Co clusters are formed, which get diffused inside the C_{60} film, leading to an inhomogeneous distribution of interparticle distance. Thus, a broad peak appears at lower-thickness Co films, while in the case of sample S3, the position of the peak is at $q_y = 0.095\ \text{Å}^{-1}$, which shifts towards lower $q_y = 0.078\ \text{Å}^{-1}$ for sample S4. The positions of the peaks correspond to the lateral spacings $(D = 2\pi/q_y)$ of about 66 and 80 Å in samples S3 and S4, respectively. This change in peak position suggests an increase in the average center-to-center distance of the existing Co clusters, primarily due to nearby clusters' coalescence yielding a Volmer-Weber–type growth of Co clusters [40].

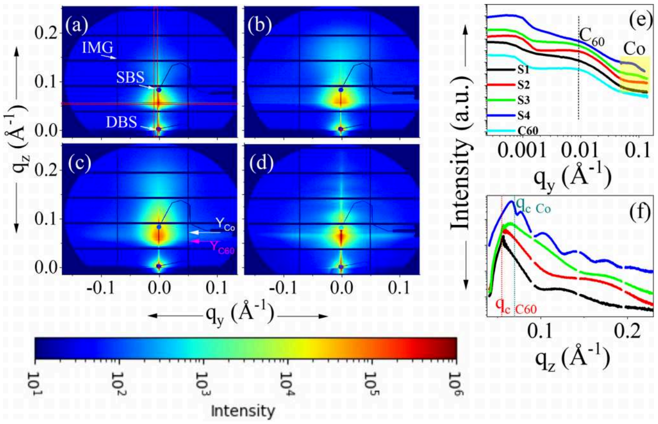

FIG. 3. (a)–(d) show characteristic GISAXS scattering patterns of samples S1–S4. (e), (f) $I(q_y)$ and $I(q_z)$ intensity profiles for all the samples extracted from the red outlined regions indicated in image (a). Both intensity and q_y are in the logarithmic scale in (e).

It is to be noted that the variations in the intensity pattern along the vertical direction is mainly due to the form-factor contribution, which strongly depends on the shape of the clusters. Hence, the modulations in the scattering intensity along the q_z direction depend on the shape of the nanoparticles. The oscillations appearing along the q_z direction as shown in Fig. 3(f) are mainly related to the growth of Co film. The distance between the two adjacent peaks along the q_z direction is equivalent to the Co film thickness. The effective thickness obtained for sample S4 is 160 ± 5 Å, which nearly matches the Co_{top} thickness obtained after the XRR fitting. Another fascinating feature of the scattering profiles $I(q_z)$ is observed where the intensity shifts from lower to higher q_z values, as shown in Fig. 3(f). The region known as the Yoneda peak is observed at the material-specific critical angle (α_c). This angle is determined by the real part of the x-ray refractive index (δ), where $\alpha_c = \sqrt{(2\delta)}$. Notably, δ is directly related to the average electron density of the material. The theoretically calculated values of the critical angle α_c for Co (density: 8.9 /cm³) and C_{60} (density: 1.65 g/cm³) at 12.11 keV are 0.276° and 0.123°, respectively. Thus, the corresponding q_c values for cobalt and C_{60} are, respectively, 0.072 and 0.056 Å^{-1} for an incident angle of 0.4°, also marked by dotted lines in Fig. 3(f). Thus, the shift in the peak position corresponds to the increased electron density at the interface yielding a shift from the formation of intermixed Co/C_{60} layers to more continuous Co films.

Based on the obtained GISAXS patterns, the hemispherical shape of the growing Co clusters on the C_{60} layer is considered to evaluate the size of the clusters in samples S3 and S4. Utilizing the model given by Schwartzkopf *et al.*, the average diameter of the Co clusters is calculated to be approximately 64 and 150 Å for samples S3 and S4, respectively [40]. If the dimensions of the Co clusters match the interparticle distance, the percolation of Co clusters begins. If the dimensions of the Co clusters are larger than the interparticle distances, the clusters overlap with each other. The calculated dimensions of Co clusters and interparticle separation indicate that the Co film in sample S3 lies in the percolation stage or connecting islands, while in sample S4 a continuous film of the Co has been formed.

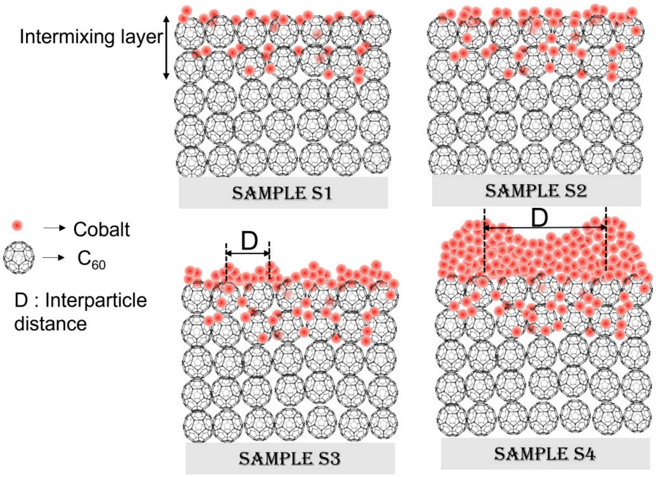

FIG. 4. Schematic of the growth evolution of the Co atoms (red balls) on the C_{60} layer (black buckyballs) for samples S1–S4.

Figure 4 shows the schematic diagram to visualize the different growth stages of the Co film on C_{60} layer observed for different samples. When metal atoms are deposited on the C_{60} layer, random diffusion on the surface takes place inside the low dense C_{60} layer. On further increasing the deposition thickness, the clusters start to agglomerate as in the case of sample S2. Since the clusters are assumed to be forming in hemispherical shape, the calculated mean diameter of the clusters in sample S3 is obtained as 64 Å. The dimensions of the formed clusters are nearly the same as that of the average corelation distance, suggesting the two Co clusters are in close contact to each other and hence, coalescence of Co clusters takes place. For higher thicknesses as in the case of sample S4, the dimensions of the clusters exceed the interparticle distance, causing the clusters to overlap with one other and forming the continuous Co film.

C. Structural studies using synchrotron-based grazing incidence wide-angle x-ray scattering and x-ray diffraction

Figure 5(a) shows the GIWAXS image collected for sample S4 simultaneously with GISAXS measurements. The overall extracted intensity profiles *I(q)* integrated radially along out-of-plane and in-plane directions are plotted in Figs. 5(b) and 5(c), respectively. For the quantitative analysis, the three peaks are fitted using a Gaussian function, and the obtained peak positions are 2.93, 3.11, and 3.30 $Å^{-1}$, which correspond to hcp (100), (002), and (101) phases of cobalt, respectively.

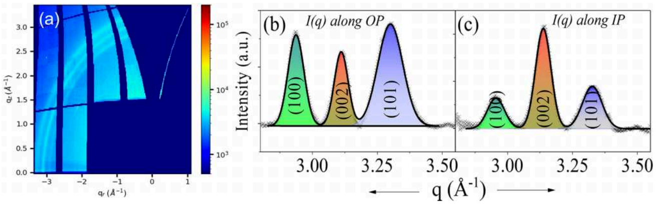

FIG. 5. (a) Two-dimensional GIWAXS images for sample S4; (b), (c) The extracted intensity profile *I*(*q*) integrated radially along out-of-plane and in-plane directions, respectively.

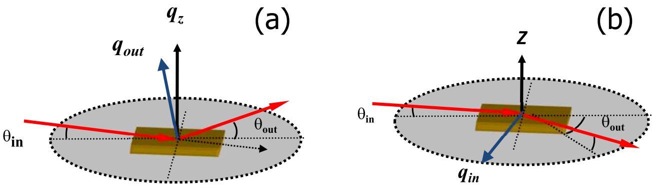

FIG. 6. (a), (b) Geometries used for the OP-XRD and IP-XRD measurements exhibiting the position of momentum transfer vector in out of plane ($q_{\rm out}$) and in plane ($q_{\rm in}$) directions.

The crystallite size corresponding to hcp (100), (002), and (101) phases of cobalt is calculated using the Debye-Scherrer formula and is found to be 83.2 ± 0.1, 95.9 ± 0.1, and 50.5 ± 0.1 Å, respectively, in the out-of-plane geometry. It is observed that there is a slight shift in the peak positions (towards higher q values) observed in the in-plane geometry, which suggests the presence of in-plane compressive stress in the Co film. Further, one can notice that the relative peak intensity shows a drastic change in both geometries. The normalized relative intensity (I_A) for Co hcp (002) is 0.20, and 0.53 is calculated along out-of-plane and in-plane directions, conveying the presence of Co film's in-plane texturing along hcp (002). To further understand the preferential texturing direction in the Co plane, XRD analysis of sample S4 is conducted using two different geometries, keeping the momentum transfer vector ($q \sim q_{\rm out}$ and $q_{\rm in}$) out of plane (OP-XRD) and in plane (IP-XRD) of the film surface. The schematic of the two geometries is depicted in Figs. 6(a) and 6(b).

In the OP-XRD setup, the incident beam strikes the sample at a shallow angle ($\theta_{\rm in} \sim 0.5°$), while the detector scans perpendicular to the film surface. This setup positions the $q_{\rm out}$ in the film's normal direction, providing information about the scattering planes nearly parallel to the film surface. On the other hand, in the IP-XRD geometry, both the incident and diffracted beams form a grazing angle of 2.8° vertically, and

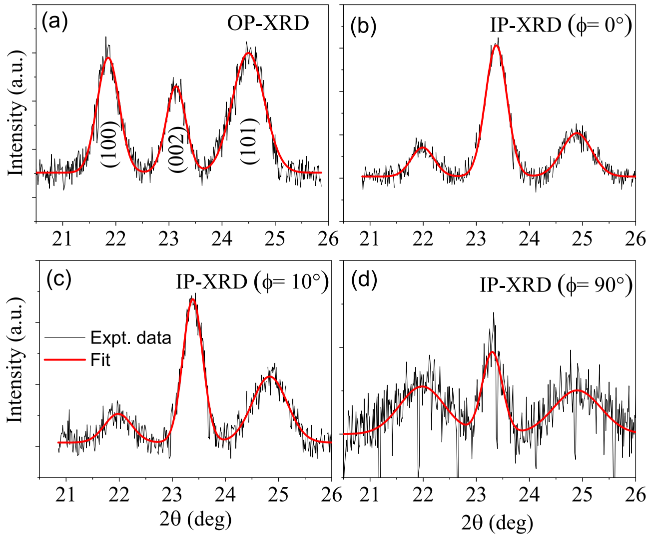

FIG. 7. (a) Fitted XRD patterns in out-of-plane geometry and (b)–(d) IP-XRD data for the momentum transfer vector ($q_{\rm in}$) along different azimuthal directions ($\phi = 0°$, 10°, and 90°) in the film plane.

TABLE II. Fitting parameters obtained from XRD patterns taken along in-plane (IP) and out-of-plane (OP) geometry for sample S4; typical error bars obtained from the least-square fitting of the XRD data approximately ±0.1% in the value of the d spacing, $d_{(002)}$.

Geometry	OP-XRD	IP-XRD ($\phi = 0^\circ$)	IP-XRD ($\phi = 10^\circ$)	IP-XRD ($\phi = 90^\circ$)
$I_{A\,(002)}$	0.21 ± 0.01	0.59 ± 0.02	0.48 ± 0.02	0.27 ± 0.06
$d_{(002)}$ (Å)	2.06	2.03	2.03	2.04
Crystallite size$_{(002)}$ (Å)	103.4 ± 3.4	95.1 ± 1.3	103.2 ± 2.1	102.6 ± 12.1

the detector scans along the plane of the film. In this setup, the momentum transfer vector (q_{in}) is almost in the plane of the film, which preferentially provides information from the scattering planes perpendicular to the film surface. Further, the q_{in} vector is rotated in the azimuthal direction to investigate the preferential orientation of Co hcp (002) grains in the film plane.

Fitted XRD patterns in OP geometry are shown in Fig. 7(a), and IP XRD patterns with momentum transfer vector (q_{in}) along $\phi = 0^\circ$, 10°, and 90° are shown in Figs. 7(b)–7(d), respectively. The OP-XRD pattern of the S4 film exhibits three distinct broad peaks corresponding to (100), (002), and (101) planes of hcp Co, while in IP-XRD, texturing along hcp (002) peak is observed. In the in-plane direction, the relative peak intensity I_A of hcp (002) is different when the direction of q_{in} within the sample plane is varied. To get qualitative information, normalized relative intensity (I_A), d spacings (d) and crystallite size corresponding to hcp (002) along different azimuthal directions are extracted after fitting the obtained XRD patterns and shown in Table II. It is important to note that the d spacings are lesser in the in-plane direction, suggesting the presence of in-plane compressive stress in Co film. Further, it can be seen from the table that the normalized relative intensity of hcp (002) is higher in the in-plane direction, suggesting the texturing of Co film along hcp (002) phase. It is to be noted that Co film is textured in the in-plane direction but preferential orientation of hcp (002) phase is observed along $\phi = 0^\circ$, which is also supported by AFM micrographs [32].

D. Angular-dependent magnetic characterizations using magneto-optic Kerr microscopy

The magnetic properties of the samples are investigated using MOKE hysteresis loops for samples S1–S4 as shown in Figs. 8(a)–8(d), and the hysteresis loops for corresponding reference samples are shown in Figs. 8(e) and 8(f). No hysteresis loop is observed at lower Co thickness, i.e., in sample S1 and S1 reference [Figs. 8(a) and 8(e)], which may be due to the formation of complex mixture of partial oxides due to higher roughness of the Co-C_{60} intermixing layer and presence of surface oxide layer in the samples. As the thickness of the Co layer increases in samples S2–S4, the hysteresis loop starts to manifest, and substantial variation in the shape of hysteresis with azimuthal angles (ϕ) is observed. Here, ϕ is defined as the angle between the nominal easy axis and the applied field direction. Along the easy axis ($\phi = 0^\circ$), the shape of the hysteresis is rectangular with a remanence ratio (M_r/M_S) close to 1, which decreases with the increasing azimuthal angle. This drastic change in the shape of the hysteresis loops indicates the presence of magnetic anisotropy in the samples S2–S4. This suggests a distinct behavior in the magnetic properties of Co films in samples S2–S4 compared to those deposited on inorganic substrates. In the case of silicon substrates, no variation in the shape of the hysteresis loops can be seen, suggesting that no magnetic anisotropy is present in samples S2$_{\text{ref}}$ and S3$_{\text{ref}}$ [shown in Figs. 8(f) and 8(g)]. The presence of magnetic anisotropy in the S4$_{\text{ref}}$ sample is demonstrated by the varying shape of the hysteresis loops along different azimuthal directions. Furthermore, one can notice a sufficiently large value of the remanent magnetization (M_r/M_S) observed along the nominal hard axis ($\phi = 90^\circ$) in sample S4. Stress is the associated cause of the magnetic anisotropy observed in polycrystalline Co films deposited on silicon substrates [28,29], which is also verified by the XRD measurements for the S4$_{\text{ref}}$ sample [32], while the observed preferential orientation of the hcp (002) in the in-plane direction suggests that the anisotropy in Co/C_{60}

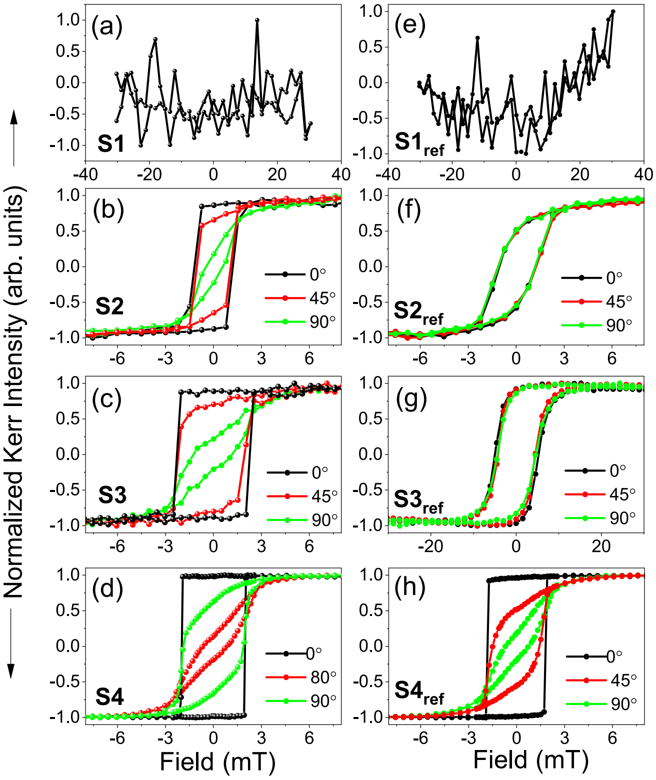

FIG. 8. (a)–(d) Hysteresis loops along different azimuthal directions for samples S1 (Co ∼ 10 Å), S2 (Co ∼ 25 Å), S3 (Co ∼ 40 Å), and S4 (Co ∼ 180 Å), respectively; (e)–(h) hysteresis loops corresponding to the reference samples S1$_{\text{ref}}$ − S4$_{\text{ref}}$, respectively. Here, azimuthal angle ϕ is defined as the angle between the easy axis and the applied field direction, i.e., $\phi = 0^\circ$ implies the magnetic field is applied parallel to the easy axis of magnetization.

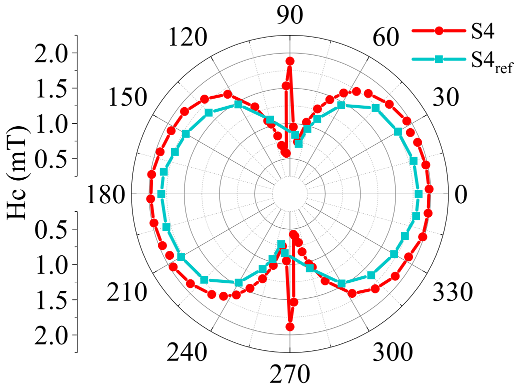

FIG. 9. Azimuthal angle-dependent coercivity (H_C) plots for samples S4 and S4$_{\mathrm{ref}}$ to compare the magnetization reversal mechanism of the Co films.

bilayers is magnetocrystalline in nature. The variation of the coercivity with azimuthal angle is shown in Fig. 9 for samples S4 and S4$_{\mathrm{ref}}$. Compared to the reference sample, sample S4 exhibits higher coercivity (H_C) values and enhanced magnetic anisotropy in the Co film attributed to the Co-C$_{60}$ interface. The presence of local maxima in the (H_C) variation is also seen at the nominal hard axis (i.e., 90°) other than 0° and 180° for sample S4 compared to the reference sample.

The azimuthal angular dependence of the M_r/M_S for samples S2–S4 is plotted in Fig. 10(a)–10(c) to understand the magnetic anisotropy and magnetization reversal mechanism in the samples. In sample S2, the variation aligns with the anticipated uniaxial anisotropy characteristics, following a $|\cos(\phi)|$ variation. This corresponds to the geometric projection of the magnetization of the easy axis onto the field axis. However, in samples S3 and S4, an anomaly is observed along the hard axis and its immediate surroundings, in addition to the cosine variation. It is seen in Figs. 10(b) and 10(c) that M_r/M_S variation displays a distinct and prominent peak centered around the nominal hard axis.

This behavior significantly diverges from the ideal Stoner-Wohlfarth single-domain particles, in which the hard axis exhibits zero remanence and coercivity as magnetization reversal is governed by coherent rotation. Further, incoherent rotation magnetization reversal mechanisms, such as fanning, curling, etc., occur in systems with additional geometrical constraints where demagnetization fields or dipolar interactions in these restricted dimensions significantly affect the reversal process and the remanence behavior [41–46]. Such extra geometrical constraints are not expected in these samples, which is also verified by GISAXS measurements as discussed above as well as from the surface topographic images obtained by SEM measurements [32]. Also, the remanence variation in these processes does not match the observed remanence behavior [47–49] shown in Figs. 10(b) and 10(c). The similar kind of anomaly, i.e., high values of the remanence and the coercivity in the hard axis, is found in polycrystalline and weakly disordered films with in-plane magnetic anisotropies [50–53]. In the present case, the dispersion in magnetic anisotropy arises due to the preferential texturing along the hcp (002) in the film plane.

The observed anomaly in the coercivity and remanence variation along the hard axis also corroborates with the domain images taken near the coercive field simultaneously with the hysteresis loop measurements using Kerr microscopy. Figure 11 shows the captured domain images near the coercive field at different azimuthal angles near the nominal hard axis for sample S4. The domain images are measured using Kerr microscopy at room temperature in longitudinal mode by varying the ϕ. Near the effective hard axis ($\phi = 80°$) no domains were observed, while at the nominal hard axis ($\phi = 90°$) the nonuniform spatial distribution of

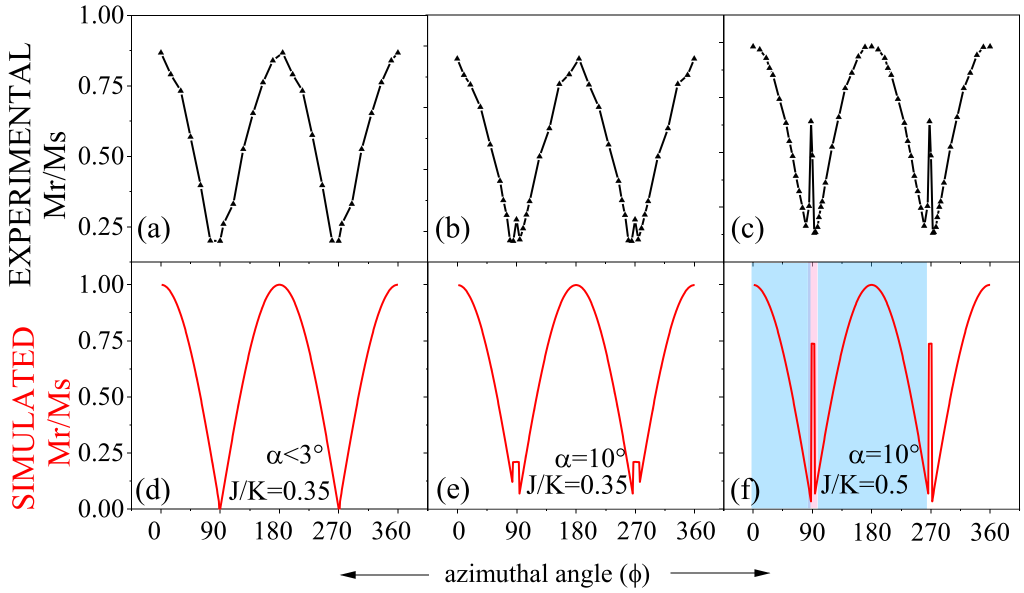

FIG. 10. (a)–(c) The experimentally obtained azimuthal angle dependence of M_r/M_S; (d)–(f) simulated azimuthal angle dependence of M_r/M_S for samples S2, S3, and S4, respectively. The different shades shown in (f) exhibit angular regions having different magnetization reversal process.

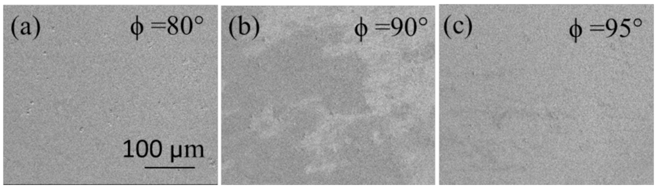

FIG. 11. Domain images near the coercivity for samples S4 at different azimuthal angles (near the nominal hard axis) are shown in (a)–(c), respectively. The scale bar for the images is shown in (a). The direction of magnetic field applied is vertical in all the images shown.

magnetization is observed. The domain images obtained along the nominal hard axis from Kerr microscopy measurements further indicates the appearance of large values of coercivity and remanence at the nominal hard axis. Thus, the observed Kerr microscopy images further confirm the dispersion in magnetic anisotropy in sample S4.

E. Theoretical understanding using two-grain Stoner Wohlfarth model

To gain insight into how the deviation in local anisotropy causes nonideal behavior in H_C and M_r/M_S variation along the hard axis, a two-grain Stoner-Wohlfarth (SW) model approach was utilized with intergranular exchange coupling and misalignment in the grain axis [50–52]. For this, we minimize the energy of the system with two different magnetic grains having anisotropy energy, Zeeman energy, and exchange energy. The energy of the system with two grains having equal normalized magnetization (i.e., $\mathbf{M_{S1}} = \mathbf{M_{S2}} = 1$) is given as

$$E = J\cos(\theta_1 - \theta_2) + H\,[\cos(\theta_1 - \phi) + \cos(\theta_2 - \phi)] + \tfrac{1}{2}K[\sin^2(\theta_1 - \alpha/2) + \sin^2(\theta_2 + \alpha/2)],$$

where J represents the constant for intergranular exchange coupling between two grains in the Co film, H is the applied magnetic field, K is the uniaxial magnetocrystalline anisotropy constant, α is the misalignment between easy axes (EA) of two grains, ϕ is the azimuthal angle between the nominal easy axis and applied magnetic field, and θ_1 and θ_2 are the angles that magnetization vectors $\mathbf{M_{S1}}$ and $\mathbf{M_{S2}}$ make with the nominal easy axis ($\phi = 0°$). The M_r/M_S variation is then simulated for two-grain system with $J/K = 0.35$, $\alpha < 3°$; $J/K = 0.35$, $\alpha = 10°$; and $J/K = 0.5$, $\alpha = 10°$, as shown in Figs. 10(d)–10(f), respectively, which matches well with the experimental results.

The schematic of the rotation of magnetization vectors $\mathbf{M_{S1}}$ and $\mathbf{M_{S2}}$ in the two-grain system upon applying a magnetic field is represented in Fig. 12(a). When the system is in a remanent state, in the absence of exchange coupling between the two grains, $\mathbf{M_{S1}}$ and $\mathbf{M_{S2}}$ align themselves at θ_1 and θ_2 such that $\theta_1 = +\alpha/2$ and $\theta_2 = -\alpha/2$ equals to

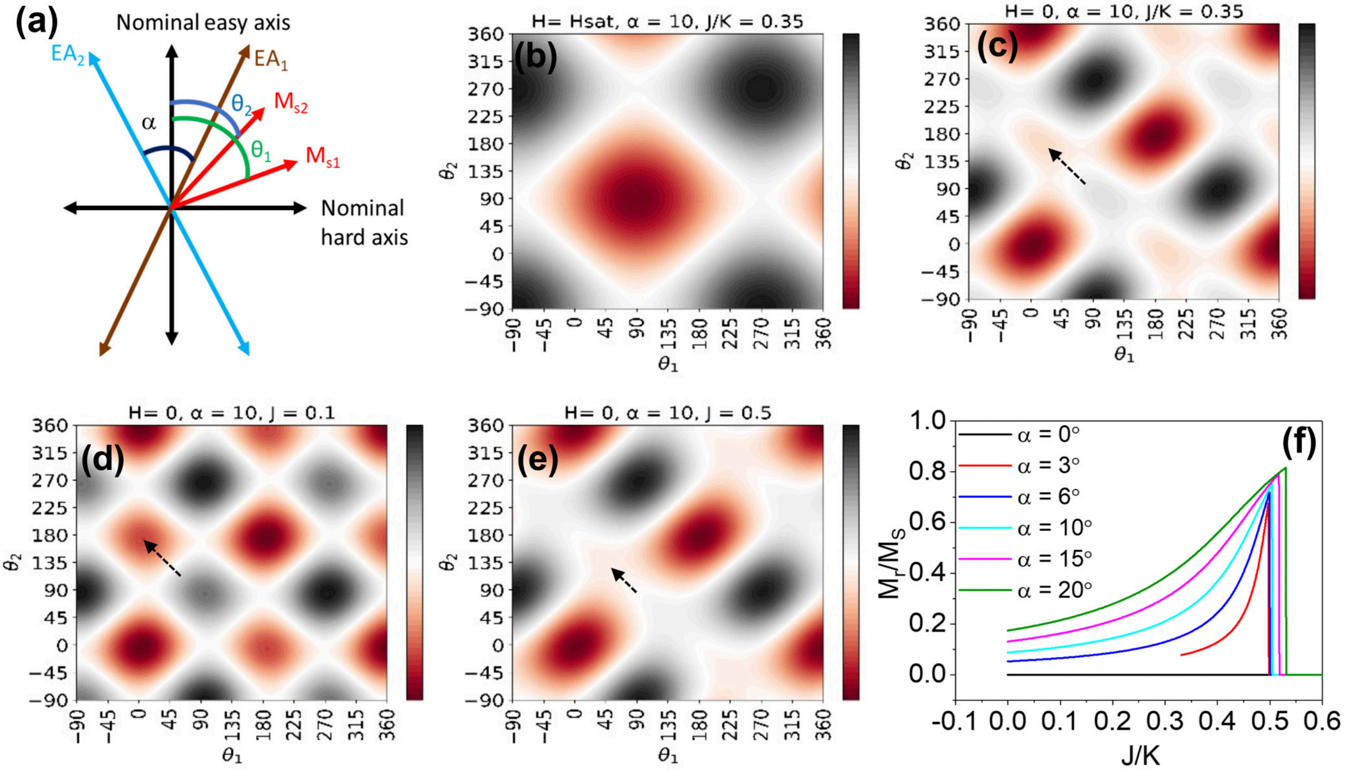

FIG. 12. (a) Rotation of magnetization vectors in a two-grain system upon application of a magnetic field. (b) Simulated energy contour plots for the two-grain system (with misalignment $\alpha = 10°$ and $J/K = 0.5$) on applying saturation field towards nominal hard axis ($\phi = 90°$). (c)–(e) Simulated energy contour plots without any external applied field for misalignment angle of 10° with varying ratios of *J/K*. The dotted arrows marked show the position of local minima. (f) Variation of M_r/M_S with *J/K* ratio for different values of misalignment angle between two easy axes.

$\pm\alpha/2$ respectively. On increasing the intergranular exchange coupling, i.e., increasing the value of *J/K* ratio, the position of θ_1 and θ_2 changes in such a way that $\theta_1 - \theta_2 < \alpha$, i.e., $0 < \theta_1 < \alpha/2$ and $-\alpha/2 < \theta_2 < 0$. When we apply magnetic field in a direction, both the $\mathbf{M_{S1}}$ and $\mathbf{M_{S2}}$ rotate to align themselves in the direction of the magnetic field. The unusual angular variation in the remanence is due to difference in the magnetization reversal process in different angular regions shown by different shaded areas in Fig. 10(f): (1) when the applied field is along $\phi \lesssim 80^\circ$ to the easy axis and (2) when the applied field is along $80^\circ \lesssim \phi \lesssim 95^\circ$. The detailed explanation of this unusual variation is discussed using the theoretical simulations of energy contour plots by considering the case when the $J/K = 0.35$ and $\alpha = 10^\circ$. On applying the magnetic field parallel to the easy axis of magnetization (i.e., $\phi = 0^\circ$) such that applied field (H_{app}) $\geqslant$ saturation field (H_{sat}), the magnetization vectors $\mathbf{M_{S1}}$ and $\mathbf{M_{S2}}$ align with the direction of applied field direction, thereby minimizing the energy of the system. After the removal of the applied field, magnetization vectors rotate back to the nearest minima in the energy landscape, i.e., (θ_1, θ_2) $\sim$ (2.94°, −2.94°), one of the global energy minima of the system. The same kind of behavior in the magnetization reversal is observed until the applied field makes angle $\phi \lesssim 80^\circ$ to the easy axis. Similarly, on applying the magnetic field ($H_{\text{app}} \geqslant H_{\text{sat}}$) towards nominal hard axis (i.e., $\phi = 90^\circ$), energy minimum/point of stability occurs almost around (θ_1, θ_2) $\sim$ (90°, 90°) as shown in Fig. 12(b). But, on decreasing the magnetic field, instead of moving to a global minimum, the magnetization vectors rotate in an opposite manner and reach local minima at $\theta_1 = 15.64^\circ$ and $\theta_2 = 164.38^\circ$, respectively, as shown in Fig. 12(c). Since the remanent magnetization in a sample can be understood as the projection of the magnetization onto the field axis after removing the applied field, the effective magnetization of the system becomes nonzero. Thus, in the remanence plot, instead of observing minima at $\phi = 90^\circ$, a sharp peak is observed at the nominal hard axis, as shown in Figs. 10(b) and 10(c).

It is important to note that no significant peak is observed at the hard axis up to a critical misalignment angle and beyond a maximum intergranular exchange coupling. The position of local minima in the energy landscape shifts towards larger values of θ_1 and smaller value of θ_2 on increasing the intergranular exchange coupling constant for a particular value of misalignment angle, which can be seen in Figs. 12(d) and 12(e). The shift in the position of local minima results in the enhancement of the anomalous peak height at the nominal hard axis. Figure 12(f) displays the simulation of the variation of the M_r/M_S with *J/K* ratio for different values of the α. This figure clearly shows that the M_r/M_S value at the nominal hard axis is sensitive to the *J/K* ratio and misalignment angle α, which leads to the modifications in the position of local minima and the alignment of magnetization vectors (θ_1, θ_2). The critical value of the misalignment angle is around $\alpha_c \sim 3^\circ$. Further, for $\alpha_c = 3^\circ$, if *J/K* ratio exceeds 0.498, the intergranular exchange coupling energy is so dominant that it compensates for the misalignment of the anisotropy axes such that both $\mathbf{M_{S1}}$ and $\mathbf{M_{S2}}$ display the same rotation during magnetization reversal process. In that case, the system resembles the behavior of the single-grain SW model. One can also notice that the critical value of *J/K* for which the modified two-grain system behaves like the single-grain SW model increases with increase in the misalignment angle.

In case of sample S2, due to the lower Co thickness the misalignment angle between the Co grains is assumed to be less than critical misalignment angle (∼3°). This is corroborated with the broad peak observed in the GISAXS intensity line profile confirming the distribution in the size of the Co clusters, which are closer to each other such that the misalignment in the magnetization vectors is very small, while on increasing thickness in samples S3 and S4, with the increase in the size of clusters, the interparticle distance also increases and hence, the misalignment angle increases. It is also noted that the intergranular exchange coupling increases in sample S4, which is due to higher density of the deposited Co film. Even though we have considered the two-grain system, it is possible that the polycrystalline Co film may comprise multiple grains with varying misalignment angles, aligning with the anisotropy dispersion. It is the random diffusion of Co film inside the C_{60} layer which induces the preferential texturing of Co film in the in-plane direction, leading to dispersion in the local grain anisotropy. Hence, the presence of nonmagnetic impurities of the C_{60} clusters at the Co-C_{60} interface as well as the preferential orientation of Co hcp (002) due to the unique morphology of the C_{60} molecular layer is the attributed cause of the unconventional magnetic anisotropy of the Co film in these bilayer structures.

IV. CONCLUSIONS

The present study illustrates the growth-induced evolution as well as the impact of Co-C_{60} interface on the structural and magnetic properties of the deposited Co film on the C_{60} layer. Unlike inorganic silicon substrates, magnetic anisotropy begins to develop at deposition thickness of Co around 25 Å on the C_{60} layer. At higher Co thicknesses, various anomalies are observed in Co/C_{60} bilayers, including remanence and coercivity variation, as well as the formation of magnetic domains near the hard axis of magnetization. These anomalies are attributed to the distribution of magnetocrystalline anisotropy due to the Co/C_{60} interface, as supported by domain imaging showing a nonuniform spatial distribution of magnetic domains. The unusual behavior of magnetic anisotropy is understood using a theoretical approach based on the simulations of energy landscape for a two-grain Stoner-Wohlfarth model, which considers varying misalignment angles and exchange coupling constants between multiple magnetic grains. The present study investigates the role of morphology and structure of the Co/C_{60} interface on the magnetic properties, which could be advantageous in tailoring Co- and C_{60}-based organic spin-valve devices. Gaining a comprehensive understanding of magnetic anisotropy in metal-organic thin films and developing effective control over it will empower researchers to optimize film properties and optimize their functionality.

ACKNOWLEDGMENTS

Financial support from the Department of Science and Technology, Government of India (Project No. CRG/2021/003094) and travel support within the framework of the India@DESY collaboration is gratefully acknowledged. Parts of this research were carried out at the P03 beamline of PETRA III at DESY, a member of the Helmholtz Association HGF. Thanks to Dr. R. Venkatesh and Mr. Mohan Gangrade for the AFM measurements. Authors also acknowledge Dr. Mukul Gupta and Ms. Akshaya A for deposition of metallic films.

---

[1] D. Sun, L. Yin, C. Sun, H. Guo, Z. Gai, X.-G. Zhang, T. Z. Ward, Z. Cheng, and J. Shen, Giant magnetoresistance in organic spin valves, Phys. Rev. Lett. **104**, 236602 (2010).

[2] Z. H. Xiong, D. Wu, Z. Valy Vardeny, and J. Shi, Giant magnetoresistance in organic spin-valves, Nature (London) **427**, 821 (2004).

[3] J. Devkota, R. Geng, R. C. Subedi, and T. D. Nguyen, Organic spin valves: A review, Adv. Funct. Mater. **26**, 3881 (2016).

[4] P. Sharangi, E. Pandey, S. Mohanty, S. Nayak, and S. Bedanta, Spinterface-induced modification in magnetic properties in $Co_{40}Fe_{40}B_{20}$/Fullerene bilayers, J. Phys. Chem. C **125**, 25350 (2021).

[5] S. Mallik, S. Mattauch, M. K. Dalai, T. Brückel, and S. Bedanta, Effect of magnetic fullerene on magnetization reversal created at the Fe/C_{60} interface, Sci. Rep. **8**, 5515 (2018).

[6] S. Mallik, A. S. Mohd, A. Koutsioubas, S. Mattauch, B. Satpati, T. Brückel, and S. Bedanta, Tuning spinterface properties in iron/fullerene thin films, Nanotechnology **30**, 435705 (2019).

[7] A. G. Khanderao, S. Kaushik, A. S. Dev, V. R. Reddy, I. Sergueev, H.-C. Wille, P. Pandit, S. V. Roth, and D. Kumar, Interface magnetism in Fe/Alq_3 bilayer; interface resolved nuclear resonance scattering studies, J. Magn. Magn. Mater. **560**, 169663 (2022).

[8] S. Kaushik, R. Raj, I. Sergeev, P. Gupta, V. R. Reddy, and D. Kumar, Depth resolved magnetic studies of Fe/^{57}Fe/C_{60} bilayer structure under x-ray standing wave condition, J. Supercond. Nov. Magn. **37**, 1181 (2024).

[9] S. Kaushik, A. G. Khanderao, Md. S. Jamal, I. Sergeev, H. C. Wille, V. R. Reddy, and D. Kumar, Study of obliquely deposited ^{57}Fe layer on organic semiconductor (Alq_3); interface resolved magnetism under x-ray standing wave, Hyperfine Interact. **242**, 24 (2021).

[10] Y.-L. Chan, Y.-J. Hung, C.-H. Wang, Y.-C. Lin, C.-Y. Chiu, Y.-L. Lai, H.-T. Chang, C.-H. Lee, Y. J. Hsu, and D. H. Wei, Magnetic response of an ultrathin cobalt film in contact with an organic pentacene layer, Phys. Rev. Lett. **104**, 177204 (2010).

[11] S. Kaushik, A. G. Khanderao, P. Gupta, V. Raghavendra Reddy, and D. Kumar, Growth of ultra-thin Cobalt on fullerene (C_{60}) thin-film: In-situ investigation under UHV conditions, Mater. Sci. Eng.: B **284**, 115911 (2022).

[12] H. Liu, J. Wang, A. Chanana, and Z. V. Vardeny, Studies of spin transport in fullerene films, J. Appl. Phys. **125**, 142908 (2019).

[13] Y. Kawasugi, T. Ujino, and H. Tada, Room-temperature magnetoresistance in organic spin-valves based on a Co_2MnSi Heusler alloy, Org. Electron. **14**, 3186 (2013).

[14] I. Angervo, M. Saloaro, H. Palonen, H. Huhtinen, P. Paturi, T. Mäkelä, and S. Majumdar, Giant magnetoresistance response in Sr_2FeMoO_6 based organic spin valves, Appl. Surf. Sci. **589**, 152854 (2022).

[15] T. S. Santos, J. S. Lee, P. Migdal, I. C. Lekshmi, B. Satpati, and J. S. Moodera, Room-temperature tunnel magnetoresistance and spin-polarized tunneling through an organic semiconductor barrier, Phys. Rev. Lett. **98**, 016601 (2007).

[16] X. Zhang, S. Mizukami, T. Kubota, Q. Ma, M. Oogane, H. Naganuma, Y. Ando, and T. Miyazaki, Observation of a large spin-dependent transport length in organic spin valves at room temperature, Nat. Commun. **4**, 1392 (2013).

[17] M. Gobbi, F. Golmar, R. Llopis, F. Casanova, and L. E. Hueso, Room-temperature spin transport in C_{60}-based spin valves, Adv. Mater. **23**, 1609 (2011).

[18] K. Bairagi, A. Bellec, V. Repain, C. Chacon, Y. Girard, Y. Garreau, J. Lagoute, S. Rousset, R. Breitwieser, Y.-C. Hu, Y. C. Chao, W. W. Pai, D. Li, A. Smogunov, and C. Barreteau, Tuning the magnetic anisotropy at a molecule-metal interface, Phys. Rev. Lett. **114**, 247203 (2015).

[19] K. Bairagi, A. Bellec, V. Repain, C. Fourmental, C. Chacon, Y. Girard, J. Lagoute, S. Rousset, L. Le Laurent, A. Smogunov, and C. Barreteau, Experimental and theoretical investigations of magnetic anisotropy and magnetic hardening at molecule/ferromagnet interfaces, Phys. Rev. B **98**, 085432 (2018).

[20] T. Moorsom, M. Wheeler, T. M. Khan, F. Al Ma'Mari, C. Kinane, S. Langridge, D. Ciudad, A. Bedoya-Pinto, L. Hueso, G. Teobaldi, V. K. Lazarov, D. Gilks, G. Burnell, B. J. Hickey, and O. Cespedes, Spin-polarized electron transfer in ferromagnet/C_{60} interfaces, Phys. Rev. B **90**, 125311 (2014).

[21] T. Moorsom, S. Alghamdi, S. Stansill, E. Poli, G. T. M. Beg, H. Fangohr, M. Rogers, Z. Aslam, M. Ali, B. J. Hickey, and O. Cespedes, π-anisotropy: A nanocarbon route to hard magnetism, Phys. Rev. B **101**, 060408(R) (2020).

[22] S. Ding, Y. Tian, H. Dong, D. Zhu, and W. Hu, Anisotropic magnetoresistance in NiFe-based polymer spin valves, ACS Appl. Mater. Interfaces **11**, 11654 (2019).

[23] A. Chumakov, C. J. Brett, K. Gordeyeva, D. Menzel, L. O. O. Akinsinde, M. Gensch, M. Schwartzkopf, W. Cao, S. Yin, M. A. Reus, M. A. Rübhausen, P. Müller-Buschbaum, L. Daniel Söderberg, and S. V. Roth, Sprayed nanometer-thick hard-magnetic coatings with strong perpendicular anisotropy for data storage applications, ACS Appl. Nano Mater. **5**, 8741 (2022).

[24] V. Shukla, C. Mukherjee, R. Chari, S. Rai, K. S. Bindra, and A. Banerjee, Uniaxial magnetic anisotropy of cobalt thin films on different substrates using CW-MOKE technique, J. Magn. Magn. Mater. **370**, 100 (2014).

[25] T. Kuschel, T. Becker, D. Bruns, M. Suendorf, F. Bertram, P. Fumagalli, and J. Wollschläger, Uniaxial magnetic anisotropy for thin Co films on glass studied by magnetooptic Kerr effect, J. Appl. Phys. **109**, 093907 (2011).

[26] P. Sharma and A. Gupta, Effect of preparation condition on the soft magnetic properties of FeCuNbSiB thin films, J. Magn. Magn. Mater. **288**, 347 (2005).

[27] V. G. Harris, K. D. Aylesworth, B. N. Das, W. T. Elam, and N. C. Koon, Structural origins of magnetic anisotropy in sputtered amorphous Tb-Fe films, Phys. Rev. Lett. **69**, 1939 (1992).

[28] A. S. Dev, D. Kumar, P. Gupta, P. Vishwakarma, and A. Gupta, Development of residual stress and uniaxial magnetic

anisotropy during growth of polycrystalline Co film, Mater. Res. Bull. **121**, 110616 (2020).

[29] D. Kumar and A. Gupta, Evolution of structural and magnetic properties of sputtered nanocrystalline Co thin films with thermal annealing, J. Magn. Magn. Mater. **308**, 318 (2007).

[30] I. Bergenti, A. Riminucci, E. Arisi, M. Murgia, M. Cavallini, M. Solzi, F. Casoli, and V. Dediu, Magnetic properties of Cobalt thin films deposited on soft organic layers, J. Magn. Magn. Mater. **316**, e987 (2007).

[31] V. Kalappattil *et al.*, Role of the magnetic anisotropy in organic spin valves, J, Sci.: Adv. Mater. Devices **2**, 378 (2017).

[32] See Supplemental Material at http://link.aps.org/supplemental/10.1103/PhysRevB.111.184426 for additional information about the samples, which also contains Refs. [54–56].

[33] R. J. Matyi, L. E. Depero, E. Bontempi, P. Colombi, A. Gibaud, M. Jergel, M. Krumrey, T. A. Lafford, A. Lamperti, M. Meduna, A. Van der Lee, and C. Wiemer, The international VAMAS project on X-ray reflectivity measurements for evaluation of thin films and multilayers Preliminary results from the second round-robin, Thin Solid Films **516**, 7962 (2008).

[34] M. Schwartzkopf, S.-J. Wöhnert, V. Waclawek, N. Carstens, A. Rothkirch, J. Rubeck, M. Gensch, J. Drewes, O. Polonskyi, T. Strunskus, A. M. Hinz, S. J. Schaper, V. Körstgens, P. Müller-Buschbaum, F. Faupel, and S. V. Roth, Real-time insight into nanostructure evolution during the rapid formation of ultra-thin gold layers on polymers, Nanoscale Horiz. **6**, 132 (2021).

[35] L. G. Parratt, Surface studies of solids by total reflection of x-Rays, Phys. Rev. **95**, 359 (1954).

[36] A. Glavic and M. Björck, GenX 3: The latest generation of an established tool, J. Appl. Crystallogr. **55**, 1063 (2022).

[37] S. Yu, G. Santoro, K. Sarkar, B. Dicke, P. Wessels, S. Bommel, R. Döhrmann, J. Perlich, M. Kuhlmann, E. Metwalli, J. F. H. Risch, M. Schwartzkopf, M. Drescher, P. Müller-Buschbaum, and S. V. Roth, Formation of Al nanostructures on Alq3: An in situ grazing incidence small angle x-ray scattering study during radio frequency sputter deposition, J. Phys. Chem. Lett. **4**, 3170 (2013).

[38] G. Benecke, G. Benecke, W. Wagermaier, C. Li, M. Schwartzkopf, G. Flucke, R. Hoerth, I. Zizak, M. Burghammer, E. Metwalli, P. Müller-Buschbaum, M. Trebbin, S. Förster, O. Paris, S. V. Roth, and P. Fratzl, A customizable software for fast reduction and analysis of large X-ray scattering data sets: Applications of the new *DPDAK* package to small-angle X-ray scattering and grazing-incidence small-angle X-ray scattering, J. Appl. Crystallogr. **47**, 1797 (2014).

[39] G. Kaune, M. A. Ruderer, E. Metwalli, W. Wang, S. Couet, K. Schlage, R. Röhlsberger, S. V. Roth, and P. Müller-Buschbaum, In Situ GISAXS study of gold film growth on conducting polymer films, ACS Appl. Mater. Interfaces **1**, 353 (2009).

[40] M. Schwartzkopf, A. Buffet, V. Körstgens, E. Metwalli, K. Schlage, Gunthard Benecke, Jan Perlich, M. Rawolle, A Rothkirch, B. Heidmann, G. Herzog, P. Müller-Buschbaum, R. Röhlsberger, R. Gehrke, N. Stribeck, and S. V. Roth, From atoms to layers: *In situ* gold cluster growth kinetics during sputter deposition, Nanoscale **5**, 5053 (2013).

[41] A. Aharoni, Angular dependence of nucleation by curling in a prolate spheroid, J. Appl. Phys. **82**, 1281 (1997).

[42] B. D. Cullity and C. D. Graham, *Introduction to Magnetic Materials* (John Wiley & Sons, Hoboken, New Jersey, USA, 2011).

[43] S. Goolaup, N. Singh, A. Adeyeye, V. Ng, and M. Jalil, Transition from coherent rotation to curling mode reversal process in ferromagnetic nanowires, Phys. Condens. Matter **44**, 259 (2005).

[44] J. Zhang, S. Zhu, J. Ming, L. Qiao, F. Li, A. Karim, Y. Peng, and J. Fu, The magnetization reversal mechanism in electrospun tubular nickel ferrite: A chain-of-rings model for symmetric fanning, Nanoscale **11**, 13824 (2019).

[45] F. E. Luborsky and C. R. Morelock, Magnetization reversal of almost perfect whiskers, J. Appl. Phys. **35**, 2055 (1964).

[46] N. Ahmad, J. Chen, S. Dawei, J. Iqbal, and X. Han, Magnetic anisotropy and magnetization reversal in Co/Cu multilayers nanowires, J. Appl. Phys. **111**, 07C119 (2012).

[47] I. S. Jacobs and C. P. Bean, An approach to elongated fine-particle magnets, Phys. Rev. **100**, 1060 (1955).

[48] N. Ahmad, J. Y. Chen, W. P. Zhou, D. P. Liu, and X. F. Han, Magnetoelastic anisotropy induced effects on field and temperature dependent magnetization reversal of Ni nanowires and nanotubes, J. Supercond. Nov. Magn. **24**, 785 (2011).

[49] G. Han, B. Zong, P. Luo, and Y. Wu, Angular dependence of the coercivity and remanence of ferromagnetic nanowire arrays, J. Appl. Phys. **93**, 9202 (2003).

[50] O. Idigoras, A. K. Suszka, P. Vavassori, P. Landeros, J. M. Porro, and A. Berger, Collapse of hard-axis behavior in uniaxial Co films, Phys. Rev. B **84**, 132403 (2011).

[51] M. Sedrpooshan, H. Ahmadvand, D. González, and S. Dijken, Magneto-optical study of anomalous magnetization reversal in the presence of anisotropy dispersion in CoPd thin films, Phys. Rev. B **98**, 214444 2018).

[52] O. Idigoras, A. K. Suszka, P. Vavassori, B. Obry, B. Hillebrands, P. Landeros, and A. Berger, Magnetization reversal of in-plane uniaxial Co films and its dependence on epitaxial alignment, J. Appl. Phys. **115**, 083912 (2014).

[53] F. Scheurer, R. Allenspach, P. Xhonneux, and E. Courtens, Magnetic coupling of structural microdomains in bcc Fe on Cu(001), Phys. Rev. B **48**, 9890 (1993).

[54] S. K. Vayalil, D. Kumar, and A. Gupta, Growth study of Co thin film on nanorippled Si(100) substrate, Appl. Phys. Lett. **98**, 123111 (2011).

[55] C.-H. Ma, J.-H. Huang, and H. Chen, Residual stress measurement in textured thin film by grazing-incidence X-ray diffraction, Thin Solid Films **418**, 73 (2002).

[56] A. K. Bera, P. Gupta, D. Garai, A. Gupta, and D. Kumar, Effect of surface morphology on magnetization dynamics of cobalt ultrathin films: An in-situ investigation, Appl. Surf. Sci. Adv. **6**, 100124 (2021).